ORIGINAL RESEARCH

# Reduction of false positives at vessel bifurcations in computerized detection of lung nodules

**Yukihiro Nomura[1], Mitsutaka Nemoto[1], Yoshitaka Masutani[2], Shouhei Hanaoka[3], Takeharu Yoshikawa[1], Soichiro Miki[1], Eriko Maeda[1], Naoto Hayashi[1], Naoki Yoshioka[4], Kuni Ohtomo[3]**

1. Department of Computational Diagnostic Radiology and Preventive Medicine, the University of Tokyo Hospital, Tokyo, Japan. 2. Graduate School of Information Sciences, Hiroshima City University, Hiroshima, Japan. 3. Department of Radiology, the University of Tokyo Hospital, Tokyo, Japan. 4. Department of Radiology, Sanno Hospital, Tokyo, Japan.

**Correspondence:** Yukihiro Nomura. Address: Department of Computational Diagnostic Radiology and Preventive Medicine, The University of Tokyo Hospital, 7-3-1 Hongo, Bunkyo-ku, Tokyo 113-8655, Japan. E-mail: nomuray-tky@umin.ac.jp

**Received:** April 3, 2014 **Accepted:** July 4, 2014 **Online Published:** July 15, 2014
**DOI:** 10.5430/jbgc.v4n3p36 **URL:** http://dx.doi.org/10.5430/jbgc.v4n3p36

## Abstract

**Objective:** We describe a new false positive (FP) reduction method based on surface features in our computerized detection system for lung nodules and evaluate the method using clinical chest computed tomography (CT) scans.

**Methods:** In our detection method, nodule candidates are extracted using volumetric curvature-based thresholding and region growing. For various sizes of nodules, we adopt multiscale integration based on Hessian eigenvalues. For each nodule candidate, two surface features are calculated to differentiate nodules and FPs at vessel bifurcations. These features are fed into a quadratic classifier based on the Mahalanobis distance ratio.

**Results:** In an experimental study involving 16 chest CT scans, the average number of FPs was reduced from 107.5 to 14.1 per case at 90% sensitivity.

**Conclusions:** This proposed FP reduction method is effective in removing FPs at vessel bifurcations.

### Key words

Surface feature, Vessel bifurcation, Lung nodule, Chest CT, Computer-assisted detection

## 1 Introduction

Lung cancer is one of the most difficult cancers to cure, and early detection is necessary to improve patient outcomes [1, 2]. Chest computed tomography (CT) can help detect lung cancer at an earlier stage than chest radiography [3]. The recent development of multidetector-row CT (MDCT) has allowed the acquisition of thin-section images of a whole lung during a single breath hold [4]. However, due to the large number of images generated by chest MDCT examination, reading by radiologists is time-consuming and may result in missed nodules. Therefore, computer-assisted detection (CAD) systems for lung nodules in chest CT images have been developed to assist radiologists.

A number of research groups have reported a variety of CAD systems for detecting lung nodules in chest CT images, including multiple grayscale thresholding [5, 6], local density maximum algorithm [7], fuzzy clustering [8], genetic algorithm

template matching of Gaussian spheres and discs [9], filters enhancing spherical structures [10-13], curved surface morphology analysis [14], and volumetric curvature-based thresholding and region growing [15]. Commercial CAD systems for detecting lung nodules in chest CT images have also been developed, including the ImageChecker CT Lung system (R2 Technology Inc., Sunnyvale, CA, USA), Lung VCAR (GE Healthcare Technologies, Waukesha, WI, USA), and Syngo Lung CAD (Siemens Medical Solutions, Erlangen, Germany).

Although these CAD systems detect lung nodules with high sensitivity, results may include false positives (FPs). These typically occur at vessel bifurcations, sharply curved vessels, artifacts due to respiratory or cardiac motion, abnormalities on the pleura (scars and fluid build-up), and so forth [16-19]. Among these, vessel bifurcations are of particular importance, and reducing FPs occurring at vessel bifurcations would considerably improve the detection performance. In our CAD system for lung nodules [20], for example, almost half the FPs occur at vessel bifurcations.

In this paper, we propose a new FP reduction method based on surface features in our CAD system for lung nodules. We then evaluate the method using 16 clinical cases.

# 2 Methods

## 2.1 Overview of detection method

Figure 1 shows a flowchart of our detection method, which consists of three steps: preprocessing, nodule candidate extraction, and FP reduction. The preprocessing step involves isotropic resampling, lung segmentation, binarization of the lung volume, and surface extraction from the binarized lung volume. The nodule candidate extraction step involves thresholding based on the shape index value and shape-index-based region growing [20]. For various sizes of nodules, we adopted multiscale integration based on Hessian eigenvalues. Finally, the FP reduction step defines two surface features and calculates them for each nodule candidate. These feature values are fed into a quadratic classifier based on the Mahalanobis distance ratio.

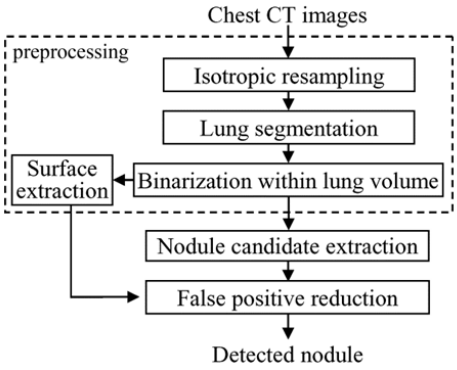


**Figure 1.** Flowchart of the detection method

## 2.2 Preprocessing

Chest CT images are resampled using trilinear interpolation to obtain the isotropic volume. The resampled voxel size is equal to the pixel size of the CT slice. After that, lung segmentation is carried out. The processing procedures of lung segmentation are described as follows:

1) The initial lung mask $\mathbf{L}_{init}$ is extracted as a set of connected voxels with CT values lower than -600 HU.
2) A gray-scale histogram of the voxels in $\mathbf{L}_{init}$ is generated, and the peak CT value in the histogram $T_{peak}$ is obtained.
3) The initial mask for the trachea and large airways is extracted as the set of connected voxels with CT values lower than $T_{peak}$ +50 HU and smoothed by opening with a spherical kernel of 2.5-voxel radius.

4) The final mask for the trachea and large airways is obtained as a superiormost connected component and dilated by a spherical kernel of 2.5-voxel radius.

5) After the removal of the mask for the trachea and large airways from the initial lung mask, closing with a spherical kernel of 5-voxel radius is applied to the masks for the left and right lungs to include lung nodules and pulmonary vessels.

6) Removal of the mask for the bones from the masks for the left and right lungs is carried out. The mask for the bones is extracted as the largest connected component with CT values higher than 100 HU, and then closing with a spherical kernel of 2.5-voxel radius and dilation with a spherical kernel of 1.5-voxel radius are carried out.

7) The lung volume **L** is obtained as the intersection voxels between the chest CT volume and the masks for the left and right lungs.

After lung segmentation, binarization within **L** is carried out again to extract the region of nodules and vessels. The binarized lung volume $\mathbf{L}_{bin}$ is given by:

$$\mathbf{L}_{bin} = \{p \mid I(\mathbf{x}) \geq T_{CT}, p \in \mathbf{L}\} \tag{1}$$

where $I(\mathbf{x})$ is the CT value (HU) of voxel $p$ and $\mathbf{x}$ is the 3D coordinate for the position of voxel $p$. $T_{CT}$ is the threshold for the extraction of vessels and nodules. Moreover, the surface areas of vessels and nodules $\mathbf{L}_{sf}$ are extracted using:

$$\mathbf{L}_{sf} = \mathbf{L}_{bin} - (\mathbf{L}_{bin} \circ \mathbf{K}_{1.0}) \tag{2}$$

where $\circ$ defines erosion and $\mathbf{K}_{1.0}$ is a spherical kernel of 1-voxel radius.

## 2.3 Extraction of nodule candidates

The shape index is calculated at the voxels of $\mathbf{L}_{bin}$ using original CT values. The shape index $S(\mathbf{x}, \sigma)$ is defined as follows [21, 22]:

$$S(\mathbf{x},\sigma) = \frac{1}{2} - \frac{1}{\pi}\arctan\frac{k_1(\mathbf{x},\sigma) + k_2(\mathbf{x},\sigma)}{k_1(\mathbf{x},\sigma) - k_2(\mathbf{x},\sigma)} \tag{3}$$

$$\begin{aligned} k_1(\mathbf{x},\sigma) &= H(\mathbf{x},\sigma) + \sqrt{H^2(\mathbf{x},\sigma) - K(\mathbf{x},\sigma)} \\ k_2(\mathbf{x},\sigma) &= H(\mathbf{x},\sigma) - \sqrt{H^2(\mathbf{x},\sigma) - K(\mathbf{x},\sigma)} \end{aligned} \tag{4}$$

where $k_1$ and $k_2$ are principal curvatures ($k_1 \geq k_2$), $H$ is the mean curvature, $K$ is the Gaussian curvature, and $\sigma$(voxel) is the standard deviation of the Gaussian filter. $S$ ranges from 0 to 1. Figure 2 shows the relation between the $S$ value and shape type. The $S$ values of the voxels of a typical nodule range from 0.8 to 1.0, showing a peak or dome, whereas those of a vessel range from 0.5 to 0.75, showing a ridge or saddle. Therefore, thresholding based on the $S$ value differentiates nodules and vessels.

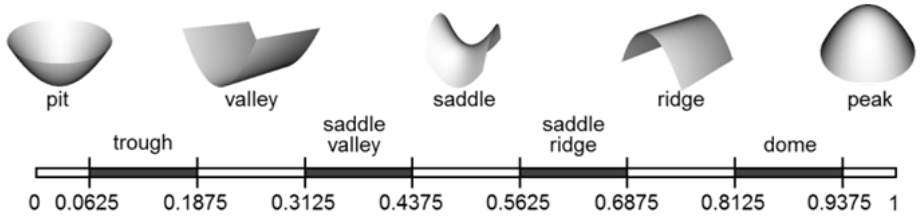


**Figure 2.** Relation between shape index value and shape type

Figure 3 shows the relationship between $\sigma/R_{eff}$ and the mean $S$ value in two isolated nodules, where $R_{eff}$ is the volume-equivalent spherical radius for the nodule. If $\sigma$ is smaller than $R_{eff}$, the mean $S$ value of nodules corresponding to the shape type of the nodule represents the "peak" value. In contrast, if $\sigma$ is larger than $R_{eff}$, the mean $S$ value is markedly degraded due to the smoothing effect of the Gaussian filter. We observed a similar tendency in 12 other isolated nodules. Multiscale integration [23] is desirable to obtain an appropriate shape index value because various sizes of nodules exist in chest CT images.

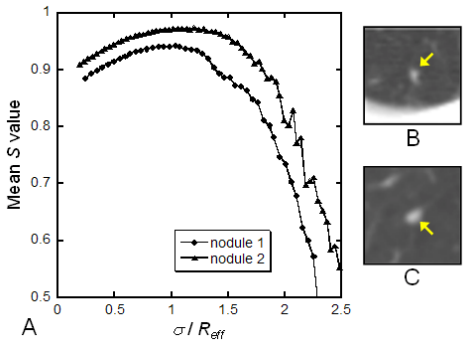


**Figure 3**. (A) Relationship between $\sigma/R_{eff}$ and mean $S$ value ($R_{eff}$: volume-equivalent spherical radius for nodule). (B) Axial section of nodule 1 ($R_{eff}$ = 2.0 voxels). (C) Axial section of nodule 2 ($R_{eff}$ = 2.7 voxels).

In this paper, we adopted multiscale integration based on Hessian eigenvalues [24, 25] to obtain $S_{opt}(\mathbf{x})$. The Hessian at voxel $p$ is given as follows:

$$\mathbf{H}(\mathbf{x},\sigma)=\begin{bmatrix} I_{xx}(\mathbf{x},\sigma) & I_{xy}(\mathbf{x},\sigma) & I_{xz}(\mathbf{x},\sigma) \\ I_{yx}(\mathbf{x},\sigma) & I_{yy}(\mathbf{x},\sigma) & I_{yz}(\mathbf{x},\sigma) \\ I_{zx}(\mathbf{x},\sigma) & I_{zy}(\mathbf{x},\sigma) & I_{zz}(\mathbf{x},\sigma) \end{bmatrix} \tag{5}$$

where the partial second derivatives of $I(\mathbf{x})$ are represented by expressions such as:

$$I_{xx}(\mathbf{x},\sigma)=\left\{\frac{\partial^2}{\partial x^2}G(\sigma)\right\}*I(\mathbf{x}) \tag{6}$$

$$I_{xy}(\mathbf{x},\sigma)=\left\{\frac{\partial^2}{\partial x\partial y}G(\sigma)\right\}*I(\mathbf{x}) \tag{7}$$

$G(\sigma)$ is a 3D Gaussian function with standard deviation $\sigma$. Let the eigenvalues of $\mathbf{H}$ be $\lambda_1$, $\lambda_2$, and $\lambda_3$ ($|\lambda_1| \geq |\lambda_2| \geq |\lambda_3|$). On the basis of these eigenvalues, a local pattern is classified as a plate-like, line-like, or blob-like structure. Table 1 summarizes the relation between $\lambda_1$, $\lambda_2$, and $\lambda_3$ for different structures. Given that the CT values of nodules and vessels are higher than those of the pulmonary parenchyma, the sign of $\lambda_1$ at a voxel within a nodule or vessel is generally negative. In our multiscale integration, Hessian eigenvalues are calculated for several values of $\sigma$, and $\sigma_{opt}(\mathbf{x})$ is determined as follows:

$$\sigma_{opt}(\mathbf{x})=\arg\min_{\sigma}\left(\sigma^{\gamma}\lambda_1(\mathbf{x},\sigma)\right) \tag{8}$$

where $\gamma$ is a parameter for normalization [23-26]. Then, $S_{opt}(\mathbf{x})$ is calculated as follows:

$$S_{opt}(\mathbf{x})=S\left(\mathbf{x},\sigma_{opt}(\mathbf{x})\right) \tag{9}$$

After calculating $S_{opt}$, the sets of connected voxels with signals higher than a given threshold of shape index value $S_{high}$ are extracted. $S_{high}$ is set to higher than 0.8 to reduce the influence of artifacts. Small components under a volume threshold $T_{size}$ are then removed. If $T_{size}$ is set too high, FPs caused by the artifacts as well as true nodules with a small size or nonspherical shape are removed. Finally, shape-index-based region growing is carried out in $\mathbf{L}_{bin}$. The termination criterion for region growing is set to $S_{low} \leq S_{opt} \leq 1.0$. $S_{low}$ is set to a value that differentiates nodules from vessels, and $S_{low} < S_{high}$.

**Table 1.** Local pattern in relation to Hessian eigenvalues

| Structure | | $\lambda_1$ | $\lambda_2$ | $\lambda_3$ |
|---|---|---|---|---|
| No noticeable structure | | • | • | • |
| Plate-like | bright | – | • | • |
| | dark | + | • | • |
| Line-like | bright | – | – | • |
| | dark | + | + | • |
| Blob-like | bright | – | – | – |
| | dark | + | + | + |

•: small eigenvalue, +: significant positive value, –: significant negative value.

## 2.4 FP reduction

In this section, we describe our FP reduction scheme developed for FPs at vessel bifurcations and its theoretical basis with examples of synthetic data analysis.

In the literature, curvature and Hessian eigenvalues, both based on second derivatives of a volumetric image function, are often employed for lung nodule detection [8, 11, 12, 14, 15, 20]. These two features have a certain relationship, derived from the fact that the principal curvatures in Equation 4 are calculated from the rotation transformation and eigenvalue analysis of the Hessian [27]. It is known that FPs in the detection of nodule-like structures based on curvature and Hessian eigenvalues also have a similar tendency.

Figure 4A shows synthetic volume data used to simulate a vessel bifurcation with Gaussian noise. The intensity levels of the vessel (foreground) and background were set to -200 and -900 HU, respectively, and the standard deviation of the Gaussian noise was 50. Figure 4B shows the shape index image. As shown in Figure 4B, the $S_{opt}$ value at the center of the vessel bifurcation is high. Figure 4C shows the region of the nodule candidate obtained by our method.

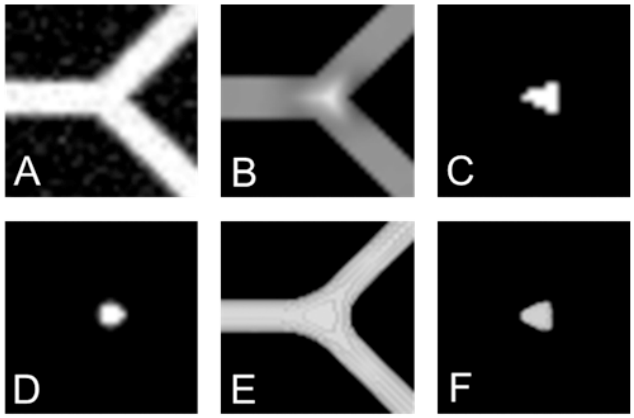


**Figure 4.** Examples of synthetic data analysis. (A) Synthetic volume data of vessel bifurcation with Gaussian noise, in which the vessel and background intensities are set to -200 and -900 HU, respectively, and the standard deviation of the Gaussian noise is 50. (B) Shape index image of A, in which a higher shape index is shown by a lighter gray-scale value. (C) Region of nodule candidate obtained by our method. (D) Enhanced image obtained by the dot-enhancement filter. (E) Isosurface of the Gaussian-smoothed image of the synthetic data (threshold: -700 HU). (F) Isosurface of the Gaussian-smoothed image of the synthetic data (threshold: -600 HU).

A similar result can be obtained using a Hessian-eigenvalue-based detection scheme. Figure 4D shows a dot-enhanced image applied to the image in Figure 4A based on Hessian eigenvalues [12]. The filter is defined as follows:

$$z_{blob}(\mathbf{x}) = \begin{cases} |\lambda_3|^2 / |\lambda_1| & \text{if } \lambda_1 < 0, \lambda_2 < 0, \lambda_3 < 0 \\ 0 & \text{otherwise} \end{cases} \quad (10)$$

As shown in Figure 4D, the center of the vessel bifurcation is enhanced by the filter, thereby yielding an FP due to its misclassification as a blob-like structure (see Table 1).

FPs at vessel bifurcations are inevitable in the detection of nodule-like structures using second-derivative-based features. This is a by-product of the Gaussian convolution employed for scale-matching. It is easily confirmed that Gaussian filtering forms or enhances a blob-like isosurface inside a vessel bifurcation (see Figures 4E and 4F). Without Gaussian filtering, however, it is impossible to obtain scale-matched features of target objects such as vessels and nodules. To remove these FPs, we utilize the spatial relationship between vessels and FPs based on the fact that the FP volume is limited to the center of a bifurcation, as shown in Figures 4B and 4D.

We first define the *surface exposure ratio* $R_{SE}$ and *surface area to volume ratio* $R_{SV}$ and calculate these features for each nodule candidate. Let $\mathbf{c}(i)$ denote the voxel set in the $i$th nodule candidate. $R_{SE}(i)$ and $R_{SV}(i)$ are defined by:

$$R_{SE}(i) = \frac{N_c(i)}{A(i)} \quad (11)$$

$$R_{SV}(i) = \frac{A(i)}{V(i)} \quad (12)$$

where $A(i)$ is the number of voxels of the surface area in $\mathbf{c}(i)$, that is, the number of voxels in $\mathbf{c}(i) - (\mathbf{c}(i) \circ \mathbf{K}_{1.0})$. $V(i)$ is the number of voxels included in $\mathbf{c}(i)$ and $N_c(i)$ is the number of intersection voxels of $\mathbf{L}_{sf}$ and $\mathbf{c}(i)$. In the case of FPs at a vessel bifurcation, $\mathbf{c}$ exists only at the center of the bifurcation (see Figures 5A-5C), while region $\mathbf{L}_{sf}$ exists only at the surface of the vessel (see Figure 5D). Therefore, $R_{SE}$ is small since $N_c$ is much smaller than $A$. $R_{SE} = 0.28$ and $R_{SV} = 0.79$ for the nodule candidate shown in Figure 5C. In contrast, in the case of a nodule, $\mathbf{c}$ includes almost the whole area of the nodule (see Figures 5E-5H). Therefore, $R_{SE}$ is close to 1.0 since $N_c$ is almost equal to $A$. $R_{SE} = 1.0$ and $R_{SV} = 0.61$ for the nodule candidate shown by Figure 5G. Figure 6A shows the $R_{SV}$ - $R_{SE}$ feature space for true positives (TPs) and FPs at the vessel bifurcation; as shown in this figure, it is expected that FPs at vessel bifurcations will be removed by using a classifier consisting of $R_{SE}$ and $R_{SV}$.

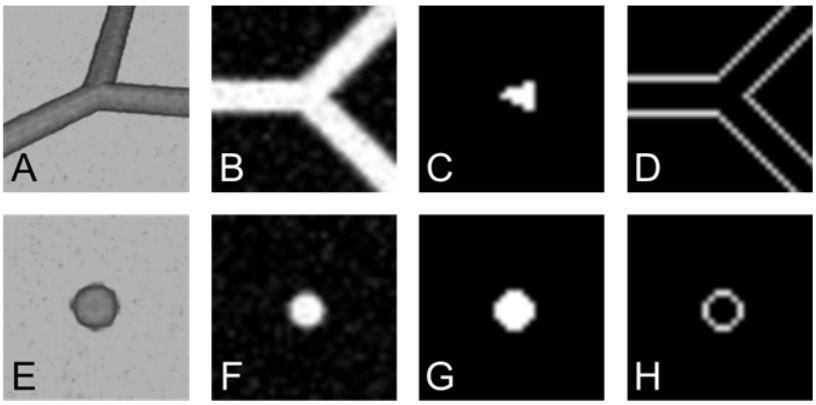


**Figure 5.** Examples of synthetic data analysis. (A) 3D volume rendering of a synthetic image of a vessel bifurcation using the same image parameters as in Figure 4A. (B) Image of an axial section of A. (C) Region of a nodule candidate obtained by our method. (D) Result of surface extraction. (E) 3D volume rendering of a synthetic image of a nodule with Gaussian noise, in which the nodule and background intensities are set to -200 and -900 HU, respectively, and the standard deviation of the Gaussian noise is 50. (F) Image of an axial section of E. (G) Region of nodule candidate obtained by our method. (H) Result of surface extraction.

The obtained values of $R_{SE}$ and $R_{SV}$ are fed into a quadratic classifier based on the Mahalanobis distance. From the Mahalanobis distance $D_j$ ($j$ = $TP$, $FP$), **c** is classified as belonging to either the TP or FP class. The Mahalanobis distance ratio $R_M$ is defined as follows:

$$R_M = \frac{D_{FP}}{D_{TP}} \tag{13}$$

If $R_M$ is below a certain threshold, **c** is classified as an FP and removed from the final results.

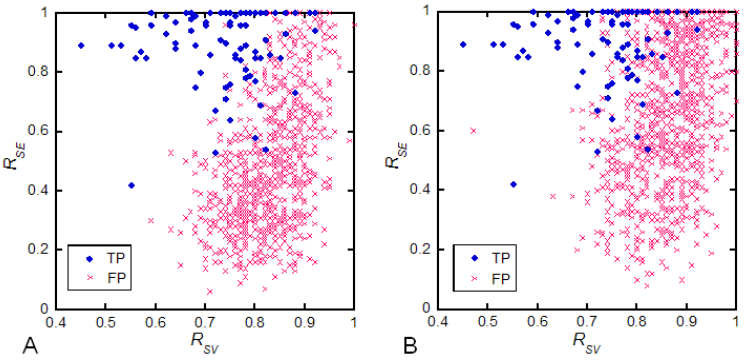


**Figure 6.** $R_{SV}$ - $R_{SE}$ feature space for $T_{CT}$ = -700, $T_{size}$ = 16, $S_{high}$ = 0.9, and $S_{low}$ = 0.8. (A) TPs and FPs at a vessel bifurcation. (B) TPs and FPs in other regions.

# 3 Results

This study was approved by the ethical review board of our institute. We evaluated the proposed FP reduction method using 16 chest CT scans acquired by MDCT scanners (Aquilion 16 or Aquilion 64, Toshiba, Tokyo, Japan). Each slice has a matrix size of 512 × 512 with a pixel size of 0.683 or 0.781 mm. The reconstruction interval is 1.0 mm. Two experienced radiologists identified 82 true nodules ranging from 3.0 mm to 12.5 mm in diameter. The nodules include four types of patterns: noncalcified solid, calcified solid, mixed ground-glass opacity (GGO), and pure GGO. Each CT scan included at least one true nodule. The performance of the detection method was evaluated using a leave-one-out cross-validation method.

In the extraction of nodule candidates, $T_{CT}$ was experimentally set to -700 in order to detect all the identified true nodules. The range of σ in multiscale integration was experimentally set to {1, 2, 3, 4, 5} in consideration of the extraction performance, as discussed later. $S_{low}$, $S_{high}$, and $\gamma$ were experimentally set to 0.8, 0.9, and 1.5, respectively.

Table 2 shows the FP reduction performance of our detection method at 80% and 90% sensitivities. As shown in Table 2, the number of FPs with $T_{size}$ = 16 was 14.1 per case at 90% sensitivity and 4.8 per case at 80% sensitivity. The number of FPs in the step for nodule candidate extraction with $T_{size}$ = 16 was 107.5 per case without false negatives (FNs). Figure 7 shows the free-response receiver operating characteristic (FROC) curves for different $T_{size}$ values.

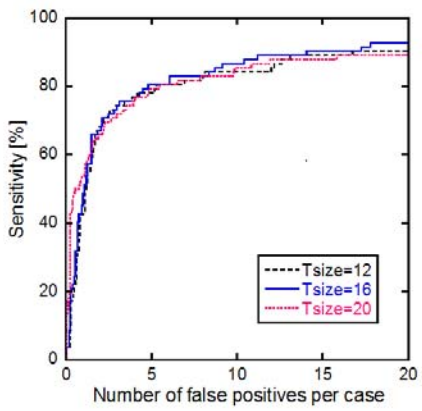


**Figure 7**. FROC curves for different $T_{size}$ values

**Table 2.** FP reduction performance of our detection method

| $T_{size}$ | Sensitivity (%) | |
|---|---|---|
| | 80 | 90 |
| 12 | 5.3 | 16.8 |
| 16 | 4.8 | 14.1 |
| 20 | 5.4 | 25.1 |

Figure 8 shows an example of a detection result using our detection method, revealing a marked reduction in FPs. Figure 9 shows an example of residual FPs in our detection method. Figure 9A shows the case of an aneurysm-like structure. Figure 9B shows the case of a mucus plug in a bronchus. Figure 10 shows an example of an FN in our detection method, which is the case of a juxtapleural nodule. A juxtapleural nodule is defined as a nodule having part of its circumference abutting a pleural surface, *i.e*., a chest wall, diaphragm, mediastinum, or fissure [28].

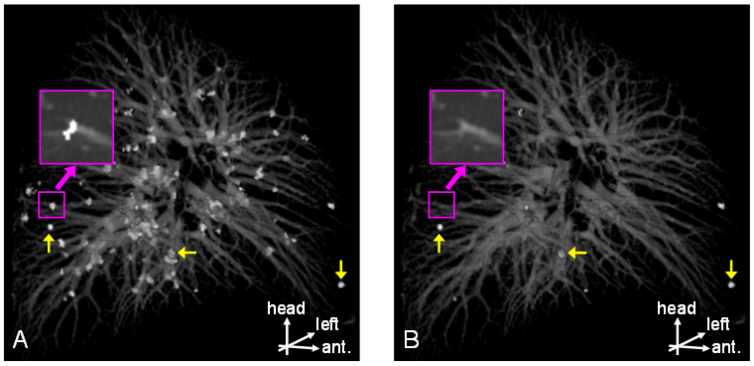


**Figure 8.** Example of detection result using our detection method. (A) Result of nodule candidate extraction with $T_{size}$ = 16. (B) Result of FP reduction at 90% sensitivity. White regions with a yellow arrow indicate true nodules, and white regions without a yellow arrow show FPs.

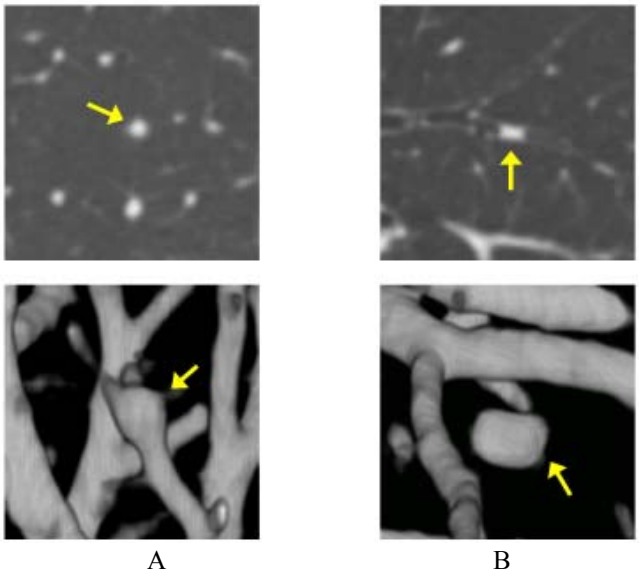


**Figure 9**. Example of residual FPs in our detection method. (A) Case of aneurysm-like structure. (B) Case of mucus plug in a bronchus. The top row shows the axial section and the bottom row shows the 3D volume rendering.

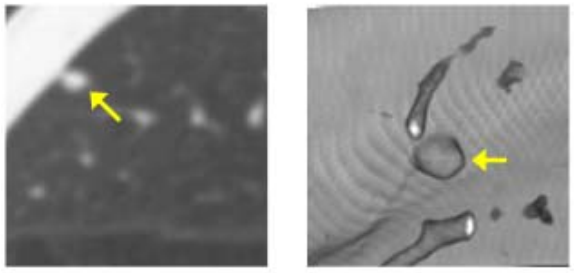

**Figure 10.** Example of FN in our detection method in the case of a juxtapleural nodule. The left image shows the axial section and the right image shows the 3D volume rendering.

# 4 Discussion

In this paper, we propose a surface-feature-based FP reduction method for eliminating FPs at vessel bifurcations. In our clinical study, the proposed method greatly contributed to reducing the number of FPs, from 107.5 to 14.1 per case at 90% sensitivity.

Many FPs with a low $R_{SE}$ value occur in other regions, such as vessel crossings or bifurcations of the bronchial wall (see Figure 6B). Consequently, our proposed method is also effective in removing FPs in other regions with low $R_{SE}$ values (see Figures 7 and 8). In addition, the proposed method is useful as an FP reduction method in Hessian-eigenvalue-based lung nodule detection (see Figure 4).

We experimentally set $T_{CT}$ = -700 to detect all the identified nodules. The appropriate $T_{CT}$ value depends on the data set. In particular, the existence of pure GGO nodules in data sets greatly affects the appropriate value of $T_{CT}$ since GGO is defined as a hazily increased attenuation of the lung observed on CT images with preservation of the bronchiole and vascular margins [29, 30].

We experimentally set the range of $\sigma$ in multiscale integration to {1, 2, 3, 4, 5}, although the maximum value of $\sigma$ is smaller than the maximum radius of a nodule. If $\sigma_{opt}$ is smaller than the radius of a nodule, the shape index of the nodule is an appropriate value corresponding to the shape type (see Figure 3). Similar methods for multiscale integration based on Hessian eigenvalues have been reported by Li *et al*. [12] and Sato *et al*. [25], in which the set of $\sigma$ was selected such that $\sigma_{k+1}/\sigma_k$ was approximately constant ($\sigma_k < \sigma_{k+1}$). We also investigated the set of $\sigma$ of {1, 1.5, 2.25, 3.375, 5} and found that the shape index decreased markedly on the surface of nodules because of the overscaling of $\sigma_{opt}$. Moreover, the selected $\sigma$ had a tendency to overscale with increasing $\gamma$ [26]. To avoid the overscaling of $\sigma_{opt}$, we therefore set $\gamma$ = 1.5.

If $T_{size}$ is set too low, FPs with a small size are extracted as nodule candidates and fed into the classifier for FP reduction, and the number of FPs increases at 90% sensitivity (see Table 2 and Figure 7). On the other hand, if $T_{size}$ is set too high, small or nonspherical true nodules are removed in nodule candidate extraction. Consequently, the value of $T_{size}$ affects the overall performance of our detection method. Further improvement of our proposed method will require additional features for the effective removal of small FPs.

The removal of the residual FPs, as shown in Figure 9, is difficult owing to their nodule-like structure. The shapes of these FPs are similar to those of TPs and their $R_{SE}$ values are close to 1.0. However, radiologists can differentiate between such FPs and true nodules by considering adjacent anatomical structures such as vessels and bronchi. Further improvement of our proposed FP reduction method will require additional features based on adjacent anatomical structures.

TPs with a low $R_{SE}$ value result in FNs, as shown in Figure 6. The $R_{SE}$ value is affected by the attachment of adjacent structures. The $N_c$ values of nodules attached to adjacent structures are smaller than those of isolated nodules since the attachment is not extracted as part of the region $\mathbf{L}_{sf}$. Hence, the $R_{SE}$ values of nodules attached to adjacent structures are smaller than those of isolated nodules. In particular, the degradation of the $R_{SE}$ value typically occurs in the case of juxtapleural nodules, as shown in Figure 10. To further reduce FPs without eliminating TPs, we are currently developing an FP reduction method based on dual classifiers for juxtapleural and nonpleural nodules. The results of preliminary experiments indicate that dual classifiers have the potential to improve the performance of FP reduction.

We conclude that the surface-feature-based FP reduction method is effective in removing FPs at vessel bifurcations.

# References

[1] Sone S, Takashima S, Li F, Yang Z, Honda T, Maruyama Y, *et al*. Mass screening for lung cancer with mobile spiral computed tomography scanner. Lancet. 1998 Apr; 351(9111): 1242-5. http://dx.doi.org/10.1016/S0140-6736(97)08229-9

[2] Nawa T, Nakagawa T, Kusano S, Kawasaki Y, Sugawara Y, Nakata H. Lung cancer screening using low-dose spiral CT: results of baseline and 1-year follow-up studies. Chest. 2002 Jul; 122(1): 15-20. PMid: 12114333. http://dx.doi.org/10.1378/chest.122.1.15

[3] Swensen SJ, Jett JR, Hartman TE, Midthun DE, Mandrekar SJ, Hillman SL, *et al*. CT screening for lung cancer: five-year prospective experience. Radiology. 2005 Apr; 235(1): 259-65. PMid: 15695622. http://dx.doi.org/10.1148/radiol.2351041662

[4] Kim JS, Kim JH, Cho G, Bae KT. Automated detection of pulmonary nodules on CT images: effect of section thickness and reconstruction interval -- initial results. Radiology. 2005 Jul; 236(1): 295-9. PMid: 15955863. http://dx.doi.org/10.1148/radiol.2361041288

[5] Giger ML, Bae KT, MacMahon H. Computerized detection of pulmonary nodules in computed tomography images. Invest Radiol. 1994 Apr; 29(4): 459-65. PMid: 8034453. http://dx.doi.org/10.1097/00004424-199404000-00013

[6] Armato SG, Giger ML, MacMahon H. Automated detection of lung nodules in CT scans: Preliminary results. Med Phys. 2001 Aug; 28(8): 1552-61. PMid: 11548926. http://dx.doi.org/10.1118/1.1387272

[7] Zhao B, Gamsu G, Ginsberg MS, Jiang L, Schwartz LH. Automatic detection of small lung nodules on CT utilizing a local density maximum algorithm. J Appl Clin Med Phys. 2003 Summer; 4(3): 248-60. PMid: 12841796. http://dx.doi.org/10.1120/1.1582411

[8] Kanazawa K, Kawata Y, Niki N, Satoh H, Ohmatsu H, Kakinuma R, *et al*. Computer-aided diagnosis for pulmonary nodules based on helical CT images. Comput Med Imaging Graph. 1998 Mar-Apr; 22(2): 157-67. http://dx.doi.org/10.1016/S0895-6111(98)00017-2

[9] Lee Y, Hara T, Fujita H, Itoh S, Ishigaki T. Automated detection of pulmonary nodules in helical CT images based on an improved template-matching technique. IEEE Trans Med Imaging. 2001 Jul; 20(7): 595-604. PMid: 11465466. http://dx.doi.org/10.1109/42.932744

[10] Miwa T, Kako J, Yamamoto S, Matsumoto M, Tateno Y, Iinuma T, *et al*. Automatic detection of lung cancers in chest CT images by the variable N-Quoit filter. Systems and Computers in Japan. 2002 Jan; 33(1): 53-63. http://dx.doi.org/10.1002/scj.1099

[11] Chang S, Emoto H, Metaxas DN, Axel L. Pulmonary micronodule detection from 3D chest CT. Lecture Notes in Computer Science. 2004 Sep; 3217: 821-8. http://dx.doi.org/10.1007/978-3-540-30136-3_100

[12] Li Q, Sone S, Doi K. Selective enhancement filters for nodules, vessels, and airway walls in two- and three-dimensional CT scans. Med Phys. 2003 Aug; 30(8): 2040-51. PMid: 12945970. http://dx.doi.org/10.1118/1.1581411

[13] Matsumoto S, Kundel HL, Gee JC, Gefter WB, Hatabu H. Pulmonary nodule detection in CT images with quantized convergence index filter. Med Image Anal. 2006 Jun; 10(3): 343-52. PMid: 16542867. http://dx.doi.org/10.1016/j.media.2005.07.001

[14] Taguchi H, Kawata Y, Niki N, Satoh H, Ohmatsu H, Kakinuma R, *et al*. Lung cancer detection based on helical CT images using curved surface morphology analysis. Proc. SPIE 3661, Medical Imaging. 1999: Image Processing, 1307 (May 21, 1999).

[15] Dehmeshki J, Ye X, Valdivieso M, Roddie M Costello J. Shape based region growing using derivatives of 3D medical images: application to automatic detection of pulmonary nodules. Proceedings of the 3rd International Symposium on Image and Signal Processing and Analysis (ISPA 2003). 18-20 Sep 2003; 2: 1118-23.

[16] Wiemker R, Rogalla P, Blaffert T, Sifri D, Hay O, Srinivas Y, *et al*. Computer-aided detection (CAD) and volumetry of pulmonary nodules on high-resolution CT data. Medicamundi. 2003 Nov; 47(3): 37-44.

[17] McCulloch CC, Kaucic RA, Mendonça PR, Walter DJ, Avila RS. Model-based detection of lung nodules in computed tomography exams. Thoracic computer-aided diagnosis. Acad Radiol. 2004 Mar; 11(3): 258-66. http://dx.doi.org/10.1016/S1076-6332(03)00729-3

[18] Das M, Mühlenbruch G, Mahnken AH, Flohr TG, Gündel L, Stanzel S, *et al*. Small pulmonary nodules: effect of two computer-aided detection systems on radiologist performance. Radiology. 2006 Nov; 241(2): 564-71. PMid: 17057074. http://dx.doi.org/10.1148/radiol.2412051139

[19] Saba L, Caddeo G, Mallarini G. Computer-aided detection of pulmonary nodules in computed tomography: analysis and review of the literature. J Comput Assist Tomogr. 2007 Jul-Aug; 31(4): 611-9. PMid: 17882043. http://dx.doi.org/10.1097/rct.0b013e31802e29bf

[20] Nomura Y, Itoh H, Maed E, Masutani Y, Yoshikawa T, Hayashi N, *et al*. Shape based automated detection of pulmonary nodules with surface feature based false positive reduction. Int J CARS 2007; 2 (Suppl. 1): S355-S357.

[21] Koenderink JJ. Solid Shape. Cambridge, MA: MIT Press. 1990.

[22] Dorai C, Jain AK. COSMOS: a representation scheme for 3D free-form objects. IEEE Trans Pattern Anal Mach Intell. 1997 Oct; 19(10): 1115-30. http://dx.doi.org/10.1109/34.625113

[23] Lindeberg T. Scale-space theory in computer vision. Dordrecht, Netherlands: Kluwer Academic Publishers. 1994. http://dx.doi.org/10.1007/978-1-4757-6465-9

[24] Lorenz C, Carlsen IC, Buzug TM, Fassnacht C, Weese J. Multi-scale line segmentation with automatic estimation of width, contrast and tangential direction in 2D and 3D medical images. Lecture Notes in Computer Science. 1997 Mar; 1205: 233-42. http://dx.doi.org/10.1007/BFb0029242

[25] Sato Y, Nakajima S, Shiraga N, Atsumi H, Yoshida S, Koller T, *et al*. Three-dimensional multi-scale line filter for segmentation and visualization of curvilinear structures in medical images. Med Image Anal. 1998 Jun; 2(2): 143-68. http://dx.doi.org/10.1016/S1361-8415(98)80009-1

[26] Majer P. On the influence of scale selection on feature detection for the case of linelike structures. Int J Computer Vision. 2004 Dec; 60(3): 191-202. http://dx.doi.org/10.1023/B:VISI.0000036834.42685.b6

[27] Van Vliet LJ, Verbeek PW. Curvature and bending energy in digitized 2D and 3D images. Proceedings of the 8th Scandinavian Conference on Image Analysis. 1993: 1403-10.

[28] Beigelman-Aubry C, Raffy P, Yang W, Castellino RA, Grenier PA. Computer-aided detection of solid lung nodules on follow-up MDCT screening: evaluation of detection, tracking, and reading time. AJR Am J Roentgenol. 2007 Oct; 189(4): 948-55. PMid: 17885070. http://dx.doi.org/10.2214/AJR.07.2302

[29] Zhou J, Chang S, Metaxas DN, Zhao B, Schwartz LH, Ginsberg MS. Automatic detection and segmentation of ground glass opacity nodules. Lecture Notes in Computer Science. 2006 Oct; 4190: 784-91. http://dx.doi.org/10.1007/11866565_96

[30] Ikeda K, Awai K, Mori T, Kawanaka K, Yamashita Y, Nomori H. Differential diagnosis of ground-glass opacity nodules: CT number analysis by three-dimensional computerized quantification. Chest. 2007 Sep; 132(3): 984-90. PMid: 17573486. http://dx.doi.org/10.1378/chest.07-0793